Design of a broadband high-efficiency power amplifier based on a rectangular double transmission line structure

Luyu Zhang[1] , Zhiwei Zhang[1], Chenlu Wang[1] and Chao Gu[2]

[1]The School of Electronics and Information, Hangzhou Dianzi University, Hangzhou, China and [2]The ECIT Institute, Queen's University Belfast, Belfast, UK

Abstract

This paper presents a design methodology for a broadband high-efficiency power amplifier (PA). The large available impedance space of the extended continuous Class-GF mode is employed. A novel output matching network of the PA consisting of a rectangular double transmission line structure is proposed to meet impedance requirements. To validate the effectiveness of this structure, a high-efficiency PA operating in 0.8–3.0 GHz is designed using a CGH40010F GaN transistor. The measured results demonstrate that the drain efficiency falls within the range of 63.2%–71.9%, the output power varies from 40.2 to 42.2 dBm, and the gain ranges from 9.4 to 11.3 dB within the frequency band of 0.8–3 GHz. The realized PA exhibits an extremely competitive relative bandwidth of 115.8%.

Introduction

With the development of mobile communication technology, the high-order digital modulated signal with large bandwidth is usually employed to achieve higher transmission rates [1–3]. This necessitates elevated requirements for the Radio Frequency (RF) front-end circuit of the transmitter, particularly the power amplifier (PA), which is required to maintain high efficiency in a wide operating band [4–7].

Continuous mode PA theory has been proven to be an effective way to expand the operating bandwidth of PAs. Traditional continuous mode PAs such as Class-B/J mode [8], continuous Class-F mode [9] have second harmonic impedances with pure reactance, resulting in a working bandwidth with less than one octave. Similarly, although the novel continuous Class-GF mode [10] has a variable fundamental resistive impedance, a pure reactive second harmonic impedance limits the further bandwidth extension of the PAs. In order to address this challenge, the extended continuous Class-GF mode [11] is exploited in wideband PA designs. By introducing several nonlinear factors into the voltage waveforms of the continuous Class-GF mode, the load design space is significantly expanded. The fundamental and second harmonic load impedances of the extended continuous Class-GF mode have variable resistance as well as variable reactance in which there is more overlap between the fundamental impedance and the second harmonic impedance. This is beneficial for the design of broadband networks, thus realizing a high-efficiency PA with a bandwidth of more than one octave.

In order to utilize the extended continuous Class-GF mode to realize the bandwidth extension, this paper proposes a simple and effective output matching network (OMN). This novel network consists of a rectangular double transmission line structure and a harmonic modification network. Combining the extended continuous mode and the proposed OMN, a PA with high efficiency and wide bandwidth is realized.

Analysis of OMN

The extended continuous Class-GF mode has been presented in paper [11]. The output fundamental and second harmonic impedances are expressed as

$$Z_{\text{ECCGF},1}\left(\alpha, \beta, \gamma, I_{\text{m}}, \delta, \xi\right) = \left(\frac{2 - \sqrt{3}\delta}{\sqrt{3}i_{\text{ECCGF},1}}\right) + j \cdot \left[\frac{36 - 7\sqrt{3} \cdot \delta}{36 i_{\text{ECCGF},1}}\right] \cdot \xi \tag{1}$$

$$Z_{\text{ECCGF},2}\left(\alpha, \beta, \gamma, I_{\text{m}}, \delta, \xi\right) = \frac{5\sqrt{3}}{18 i_{\text{ECCGF},2}} \cdot \delta + j \cdot \frac{9\delta - 7\sqrt{3}}{18 i_{\text{ECCGF},2}} \cdot \xi \tag{2}$$

in which $i_{\text{ECCGF},1}$ is the fundamental drain current, $i_{\text{ECCGF},2}$ is the drain current of the second harmonic, and γ is the voltage ratio of the second harmonic and fundamental

voltage component at the input. In addition, δ and ξ are two parameters respectively to maintain a positive drain voltage. The remaining parameters are drain peak current (I_m), zero-crossing cutoff angle (β), and conduction angle (α).

With the aiming of achieving impedance matching, the intermediate frequency of the passband is selected as the fundamental frequency f_0, so that the fundamental impedance and the second harmonic impedance can satisfy equations (1) and (2) respectively. Since the impedance within the bandwidth varies with frequency, a rectangular double transmission line structure proposed here can be used to make the impedance of the entire passband satisfy equations (1) and (2).

In order to satisfy the impedances desired by equations (1) and (2), the harmonic control network (HCN) and the fundamental matching network (FMN) are proposed as shown in Fig. 1. To realize a wideband PA, this paper employs a rectangular double transmission line structure [12, 13] for the fundamental impedance matching. As shown in Fig. 1, transmission lines TL1, TL2, and TL3 are employed to adjust harmonic impedances expressed in equation (2). Simultaneously, these three transmission lines also play a role in fundamental impedance matching. The entire OMN is the cascade connection of HCN and FMN.

It is observed that the rectangular double transmission line structure is symmetric about the plane A-A′. The odd–even-mode analysis [14, 15] is introduced to theoretically derive the impedance of the OMN. Figure 2 depicts the equivalent circuit diagrams for odd and even modes, respectively.

As displayed in Fig. 2(a), based on the transmission line theory [16], the theoretical input odd-mode impedance $Z_{\text{in,o}}$ can be calculated as

$$Z_{\text{in,o}} = Z_{\text{o1}}//Z_{\text{o2}} = \frac{Z_{\text{o1}} \times Z_{\text{o2}}}{Z_{\text{o1}} + Z_{\text{o2}}} \tag{3}$$
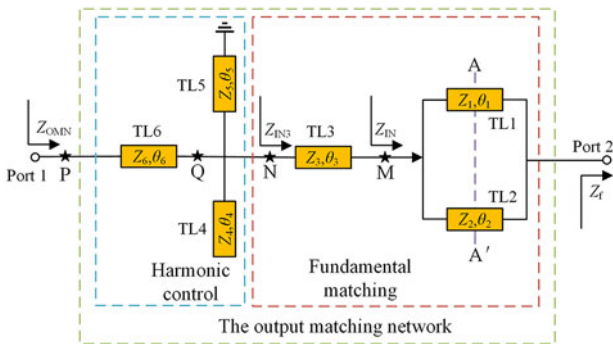

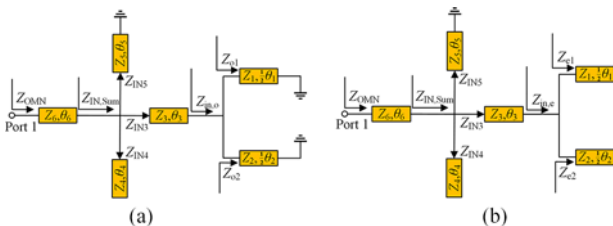**Figure 1.** Topological structure of the proposed output matching network.

Figure 2. Equivalent circuits of the output matching network: (a) odd-mode and (b) even-mode.

where

$$Z_{\text{o1}} = jZ_1\tan(\frac{1}{2}\theta_1) \tag{4}$$

$$Z_{\text{o2}} = jZ_2\tan(\frac{1}{2}\theta_2) \tag{5}$$

where θ_1, θ_2 refer to the electrical length of the transmission lines as depicted in Fig. 1. Meanwhile, Z_1, Z_2 represent the characteristic impedance of the transmission lines as depicted in Fig. 1.

As displayed in Fig. 2(b), the theoretical input even-mode impedance $Z_{\text{in,e}}$ can be derived as

$$Z_{\text{in,e}} = Z_{\text{e1}}//Z_{\text{e2}} = \frac{Z_{\text{e1}} \times Z_{\text{e2}}}{Z_{\text{e1}} + Z_{\text{e2}}} \tag{6}$$

where

$$Z_{\text{e1}} = -jZ_1\cot(\frac{1}{2}\theta_1) \tag{7}$$

$$Z_{\text{e2}} = -jZ_2\cot(\frac{1}{2}\theta_2) \tag{8}$$

According to transmission line theory [16], the impedance matrix at the point of M in the Fig. 1 can be calculated as follows:

$$[\mathbf{Z}] = \frac{1}{2}\left[\begin{array}{cc} Z_{\text{in,e}} + Z_{\text{in,o}} & Z_{\text{in,e}} - Z_{\text{in,o}} \\ Z_{\text{in,e}} - Z_{\text{in,o}} & Z_{\text{in,e}} + Z_{\text{in,o}} \end{array}\right] \tag{9}$$

Then, based on the load impedance Z_{f} of the OMN, the impedance matrix can be converted into a scattering matrix, which is expressed as follows:

$$[\mathbf{S}] = \frac{1}{2}\left[\begin{array}{cc} \frac{Z_{\text{in,e}}\cdot Z_{\text{in,o}}-Z_f}{(Z_{\text{in,e}}+Z_f)\cdot(Z_{\text{in,o}}+Z_f)} & \frac{Z_f\cdot(Z_{\text{in,e}}-Z_{\text{in,o}})}{(Z_{\text{in,e}}+Z_f)\cdot(Z_{\text{in,o}}+Z_f)} \\ \frac{Z_f\cdot(Z_{\text{in,e}}-Z_{\text{in,o}})}{(Z_{\text{in,e}}+Z_f)\cdot(Z_{\text{in,o}}+Z_f)} & \frac{Z_{\text{in,e}}\cdot Z_{\text{in,o}}-Z_f}{(Z_{\text{in,e}}+Z_f)\cdot(Z_{\text{in,o}}+Z_f)} \end{array}\right] \tag{10}$$

Based on this, the input impedance of the rectangular double transmission line structure, Z_{IN}, is expressed as

$$Z_{\text{IN}} = \frac{Z_f(Z_{\text{in,e}} + Z_{\text{in,o}}) + 2Z_{\text{in,e}}Z_{\text{in,o}}}{2Z_f + Z_{\text{in,e}} + Z_{\text{in,o}}} \tag{11}$$

where Z_f represents the load impedance of the fundamental rectangular double transmission line structure.

Then, according to transmission line theory, the input impedance of the fundamental matching network Z_{IN3} at the point of N is derived as

$$Z_{\text{IN3}} = Z_3\frac{Z_{\text{IN}} + jZ_3\tan(\theta_3)}{Z_3 + jZ_{\text{IN}}\tan(\theta_3)} \tag{12}$$

$$Z_{\text{IN4}} = -jZ_4\cot(\theta_4) \tag{13}$$

$$Z_{\text{IN5}} = jZ_5\tan(\theta_5) \tag{14}$$

where θ_3, θ_4, θ_5, refer to the electrical length of the transmission line as depicted in Fig. 1. The Z_3, Z_4, Z_5 refer to the characteristic impedance of the transmission lines as depicted in Fig. 1.

At the point Q as shown in Fig. 1, the input impedance $Z_{\text{IN,Sum}}$ is equivalent to Z_{IN3}, Z_{IN4}, Z_{IN5} in parallel.

$$Z_{\text{IN,Sum}} = Z_{\text{IN3}}//Z_{\text{IN4}}//Z_{\text{IN5}} \tag{15}$$

When $Z_{\text{IN,Sum}}$ is obtained, the input impedance Z_{OMN} at the point of P can be obtained as

$$Z_{\text{OMN}} = Z_6\frac{Z_{\text{IN,Sum}} + jZ_6\tan(\theta_6)}{Z_6 + jZ_{\text{IN,Sum}}\tan(\theta_6)} \tag{16}$$
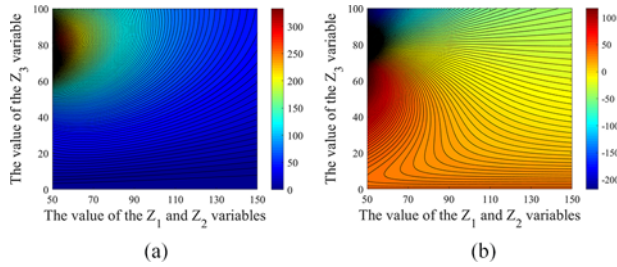
Figure 3. (a) Real part of Z_{OMN}. (b) Imaginary part of Z_{OMN}, when $\theta_1 = 90°$, $\theta_2 = 50°$, $\theta_3 = 40°$.
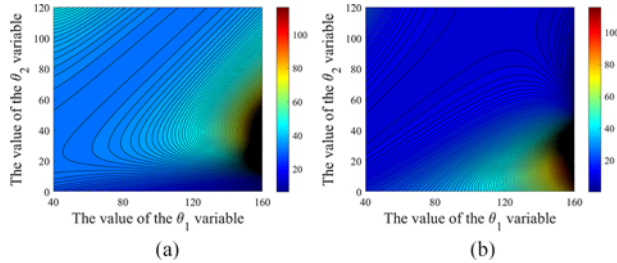

Figure 4. (a) Real part of Z_{OMN}. (b) Imaginary part of Z_{OMN}, when $Z_1 = Z_2 = 100\ \Omega$, $Z_3 = 35\ \Omega$, $\theta_3 = 40°$.

Figure 5. (a) Real part of Z_{OMN}. (b) Imaginary part of Z_{OMN}, when $Z_1 = Z_2 = 100\ \Omega$, $Z_3 = 35\ \Omega$, $\theta_2 = 50°$.
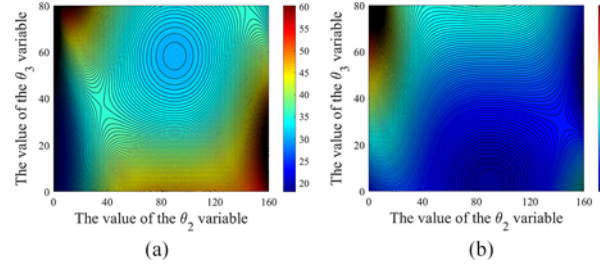

Figure 6. (a) Real part of Z_{OMN}. (b) Imaginary part of Z_{OMN}, when $Z_1 = Z_2 = 100\ \Omega$, $Z_3 = 35\ \Omega$, $\theta_1 = 90°$.

where θ_6 refers to the electrical length of the transmission line as depicted in Fig. 1. The Z_6 refer to the characteristic impedance of the transmission line as depicted in Fig. 1.

The driving point input impedance Z_{OMN} of the OMN encompasses all the parameters of Fig. 1 to be determined or selected by the designer. For the sake of simplicity, the rectangular double transmission lines are selected to have equal characteristic impedances, denoted as $Z_1 = Z_2$ in Fig. 1. The HCN has an equivalent electrical length of 90° at the second harmonic frequency $2f_0$ to cause a short circuit for the second harmonic. Therefore, the variables θ_4, θ_5, Z_4, and Z_5 are determined as 20°, 70°, 60 Ω and 70 Ω, respectively. Besides, the HCN has an equivalent electrical length of 60° at the third harmonic frequency $3f_0$ to lead to an open circuit for the third harmonic. Thus the variables Z_6 and θ_6 are taken as 50 Ω and 40°. Consequently, the electrical length of TL6, TL5, and TL4, θ_6, θ_5, and θ_4 are set as 40°, 70°, and 20°. The characteristic impedances Z_6, Z_5, and Z_4 are taken as 50 Ω, 70 Ω, and 60 Ω, respectively.

Figures 3–6 illustrate the impact of characteristic impedance and electrical length of the rectangular double transmission line structure on the impedance Z_{OMN}.

Figure 3 illustrates that the real part of the OMN impedance increases with a larger Z_3 and a smaller Z_1, Z_2. Meanwhile, the imaginary part of the impedance of the OMN decreases with increasing Z_3. As shown in Fig. 4, the impedance of the output matching network Z_{OMN} increases dramatically when θ_1 is between 120° and 160° and θ_2 varies between 0° and 80°. Outside this interval, the impedance Z_{OMN} varies smoothly. Figure 5 reveals a substantial increase in the OMN impedance when θ_1 varies between 120° and 160°. The variation in θ_3 minimally influences the real part of the OMN impedance, yet there is a slight increase in the imaginary part as θ_3 rises. From Fig. 6, it can be seen that the real part of the OMN impedance spikes for both small and large θ_2 values. As θ_2 decreases and θ_3 increases, the imaginary part of the OMN impedance grows larger.
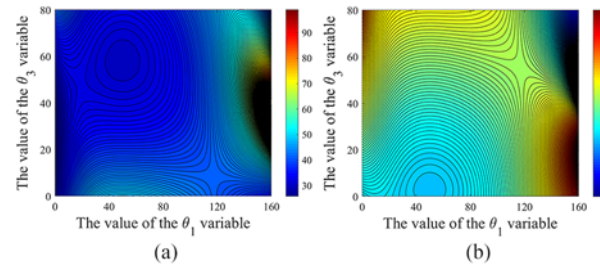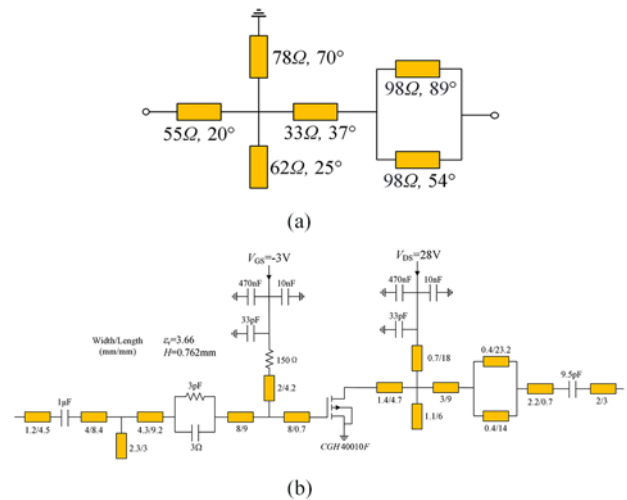

Figure 7. (a) The designed output matching network and (b) circuit schematic of the broadband high-efficiency PA.

Based on the above analysis, it is evident that the relationship between the variables has been established. Figure 3 indicates that when Z_1, Z_2, and Z_3 are within the ranges of 90–110 Ω, 90–110 Ω, and 20–40 Ω respectively, the impedance Z_{OMN} generally typically falls within the impedance solution space of equation (1). Similarly, Figs. 4–6 demonstrate that when associated with angles θ_1, θ_2, and θ_3 in the range of 40°–100°, 40°–120°, and 20°–50° respectively, the impedance Z_{OMN} typically falls within the impedance solution space of equation (1). For example, when variables Z_1, Z_2, Z_3, θ_1, θ_2, and θ_3 are respectively 100 Ω, 100 Ω, 35 Ω, 90°, 50°, and 40°, the impedance Z_{OMN} is $34.6 + j \times 11.8\ \Omega$, satisfying equation (1).

The input impedance of the rectangular double transmission line structure, Z_{IN}, is related to four parameter variables. The wider design space for these parameter variables allows for greater flexibility in achieving broadband matching. Therefore, the load
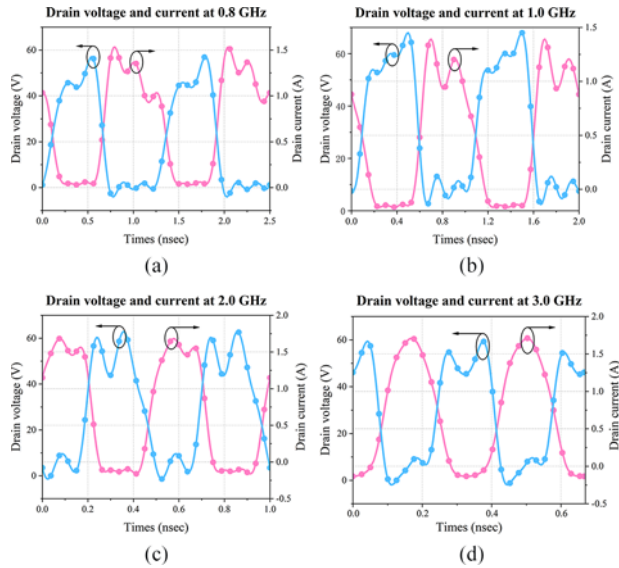
Figure 8. Simulated drain voltage and current waveforms at several frequencies: (a) 0.8 GHz, (b) 1.0 GHz, (c) 2.0 GHz, and (d) 3.0 GHz.
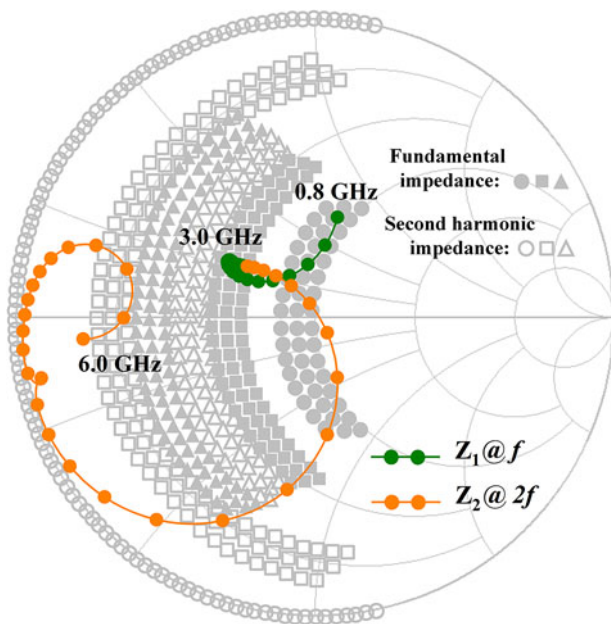

Figure 9. Simulated impedance trajectory at the I-gen plane.

impedance requirements of different PA operating modes can be satisfied by selecting the appropriate combination of parameter values, so that high efficiency can be maintained in a wide frequency band. The proposed structure is capable of satisfying the impedance requirements of various PA operating modes, such as continuous Class-F/F^{-1} mode, continuous Class-F mode, Class-B/J mode, etc. This extended continuous Class-GF mode here is just an example.

The PA circuit design and simulation

To validate the effectiveness of the proposed OMN, this work designs a high-efficiency PA operating in the frequency range of 0.8–3 GHz. The PA employs the commercial Cree CGH40010F GaN device and Rogers 4350B substrate, featuring a thickness of
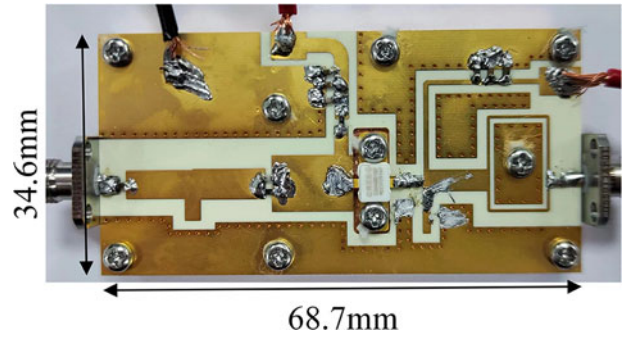

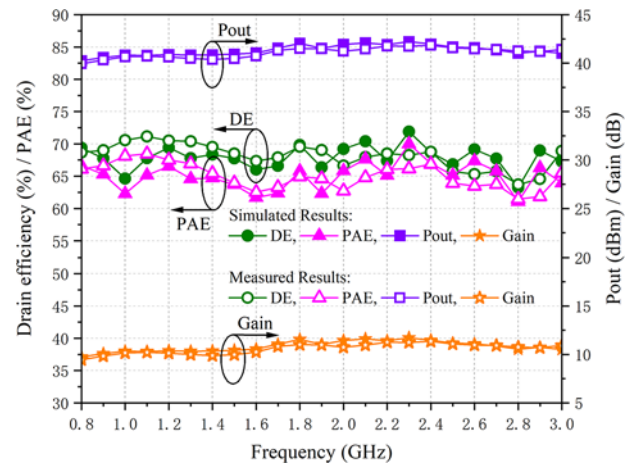**Figure 10.** Photograph of the fabricated PA.

Figure 11. Simulated and measured DE, PAE, output power, and gain across the entire bandwidth.

0.762 mm and a dielectric constant of 3.66. The DC bias voltage is set to $V_{GS} = -3$ V, and the drain DC bias voltage is set to $V_{DS} = 28$ V, enabling operating in the Class AB operation condition. Based on Figs. 3–6, the $Z_1, Z_2, Z_3, \theta_1, \theta_2, \theta_3$ are chosen as 98 Ω, 98 Ω, 33 Ω, 89°, 54°, 37° to satisfy the load impedances required by equations (1) and (2). Optimal values for these variables are determined to ensure a suitable match between the OMN and the load. Subsequently, these chosen values are integrated into the OMN and fine-tuned using ADS simulation software. Following the optimization process in ADS, the sum of the electrical lengths of TL1 and TL3 microstrip lines is less than 60°. This deviation may arise due to the small value of electrical length, which has a better effect on the impedance of third harmonics. The designed OMN is shown in Fig. 7(a). The multibranch stepped matching technique is used to design the broadband input network. The resulting comprehensive circuit schematic diagram is depicted in the Fig. 7(b).

Figure 8 displays the simulated voltage and current waveforms at several representative frequencies (0.8 GHz, 1 GHz, 2 GHz, and 3 GHz). The voltage and current waveforms have less overlap in the time domain, aligning with the expected waveform of an ideal Class-GF PA.

This simulated load impedance trajectory of the PA at the I-gen plane is illustrated in Fig. 9, the solid shadow part is the fundamental impedance region, and the hollow shadow part is the second harmonic impedance region. As observed from Fig. 9, the fundamental impedance resides within the impedance solution space of the extended continuous Class-GF mode. In addition, most of the second harmonic impedance falls in the impedance solution space,

and the part that does not fall in the impedance solution space may be caused by frequency deviation.

PA fabrication and measurement

The designed PA was fabricated based on the schematic shown in Fig. 7. A photograph of the realized PA is shown in Fig. 10.
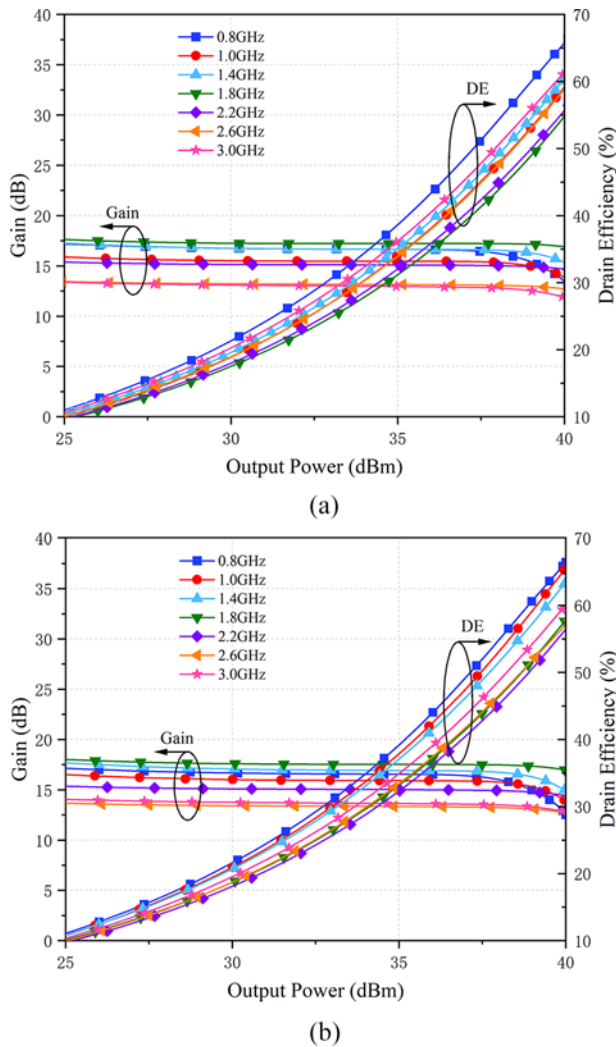

Figure 12. (a) Simulated and (b) measured DE and gain versus output power at different frequency points.

The manufactured PA underwent large-signal testing. In Fig. 11, the measurement results depict the drain efficiency (DE), output power, and gain versus working frequency of from 0.8 to 3.0 GHz. Within the operational band from 0.8 to 3.0 GHz, the PA has a DE ranging from 63.2% to 71.9%, a power-added efficiency ranging from 61.4% to 68.4%, an output power ranging from 40.2 to 42.2 dBm, and a gain ranging from 9.4 to 11.3 dB. Figure 12 illustrates the relationship between gain, DE, and output power at several representative frequencies.

As shown in Fig. 13, the PA was simulated and measured for S-parameters. Within the working bandwidth, the PA has the S11 ranging from −20.7 to −7.7 dB and the S21 ranging from 14.2 to 19.3 dB. The small signal performance of the designed PA meets the requirements.

In order to better reflect the performance of this PA, Table 1 lists several PA works. It can be seen that the designed PA exhibits characteristics of large bandwidth and high efficiency, thus verifying the effectiveness of the output-matching network structure.

Conclusion

In this paper, a PA with wide bandwidth and high efficiency is designed based on the extended continuous Class-GF mode. In order to satisfy the impedance desired by the extended continuous Class-GF mode, a novel OMN is proposed. A rectangular double transmission line structure is employed to design
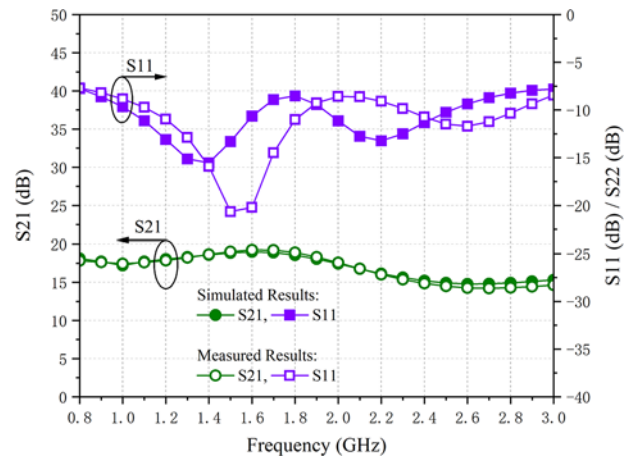
Figure 13. Simulated and measured S-parameter of the designed PA.

Table 1. Performance comparison with PAs

Ref	Class	BW/RBW (GHz/%)	DE (%)	PAE (%)	Pout (dBm)	Gain (dB)	The structure of the output matching network
[17]	CF^{-1}/CF	1.3–3.3/87	60–83	56–79	10–11	>10	ATSTLBLPMS
[18]	CCF	3.3–4.3/26	55.9–65.3	NA	39.9–40.3	NA	ALPMS
[19]	C/BJ	2.2–3.4/42	60–72.8	NA	39.6–40.4	>10	ATTLS
[10]	CCGF	3.3–4.3/26	64–68	NA	39.5–40.3	16.5–17.3	ATTLS
[20]	CCGF^{-1}	0.8–1.4/55	75–93	>73	38–42.3	>12	ATTLS
This work	**ECCGF**	**0.8–3.0/115.8**	**63.2–71.9**	**61.4–68.5**	**40.2–42.2**	**9.4–11.3**	**ARDTLS**

ATSTLBLPMS = a three-stage transmission-line-based low-pass matching structure; ALPMS = a low-pass matching structure; ATTLS = a traditional transmission line structure; ARDTLS = a rectangular double transmission line structure.

the OMN. The impedance expression and design parameters are theoretically derived. Subsequently, based on this structure and the extended continuous Class-GF mode, a high-efficiency PA with a relative bandwidth of 115.8% is implemented. The measurements reveal that the DE of 63.2%–71.9%, the power-added efficiency of 61.4%–68.4%, output power of 40.2–42.2 dBm, and gain of 9.4–11.3 dB within the frequency band of 0.8–3.0 GHz are obtained.

Competing interests. We declare that the authors have no competing interests as defined by International Journal of Microwave and Wireless Technologies or other interests that might be perceived to influence the results and/or discussion reported in this paper. The authors report no conflict of interest.

References

1. **Gustavsson U, Frenger P, Fager C, Eriksson T, Zirath H, Dielacher F, Studer C, Pärssinen A, Correia R, Matos JN, Belo D and Carvalho NB** (2021) Implementation challenges and opportunities in beyond-5G and 6G communication. *IEEE Journal of Microwaves* **1**(1), 86–100.
2. **Yao Y, Dai Z and Li M** (2024) A novel topology with controllable wideband baseband impedance for power amplifiers. *Frontiers of Information Technology & Electronic Engineering* **25**, 308–315.
3. **Du X, You CJ, Zhao Y, Li X, Helaoui M, Cai J and Ghannouchi FM** (2018) Wideband high-efficiency linearized PA design with reduction in memory effects and IMD3. *International Journal of Microwave and Wireless Technologies* **10**(4), 391–400.
4. **Cipriani E, Colantonio P, Giannini F and Giofré R** (2009) Theory and experimental validation of a Class E PA above theoretical maximum frequency. *International Journal of Microwave and Wireless Technologies* **1**(4), 293–299.
5. **Li Q** (2024) Absorptive reconfigurable bandstop filter with ultra-wide frequency tuning range using distributed lossy resonators. *International Journal of Microwave and Wireless Technologies* Published online 2024, 1–9.
6. **Hu C, Yang R, Shi W, Li L, Gao R, Dai Z, Pang J and Li M** (2023) Analysis and design of broadband outphasing power amplifier based on complex combining impedance. *IEEE Transactions on Circuits and Systems I: Regular Papers* **70**(4), 1542–1554.
7. **Liu W, Du G and Li G** (2022) Analytical dual-band matching approach for concurrent high-efficiency power amplifiers. *IEEE Transactions on Circuits and Systems II: Express Briefs* **69**(12), 4769–4773.
8. **Du X, You CJ, Cai J, Helaoui M, Ghannouchi FM, Zhao Y and Li X** (2018) Novel design space of load modulated continuous Class-B/J power amplifier. *IEEE Microwave and Wireless Components Letters* **28**(2), 156–158.
9. **Merrick BM, King JB and Brazil TJ** (2014) A novel continuous Class-F mode Power Amplifier. In *2014 IEEE Topical Conference on Power Amplifiers for Wireless and Radio Applications (PAWR)*, Newport Beach, CA, USA, 19–21.
10. **Eskandari S and Kouki AB** (2022) The second source harmonic optimization in continuous Class-GF power amplifiers. *IEEE Microwave and Wireless Components Letters* **32**(4), 316–319.
11. **Xuan X, Cheng Z, Gong T, Liu G and Le C** (2023) Design of an extended continuous-mode Class-GF power amplifier with multioctave bandwidth. *IEEE Microwave and Wireless Technology Letters* **33**(9), 1329–1332.
12. **Li L, An T-T, Wang W-W and Zhang W-M** (2008) A square ring dual-band filter with adjustable second-passband by the open stubs. In *2008 International Conference on Microwave and Millimeter Wave Technology*, Nanjing, 291–293.
13. **Doan M, Che W and Nguyen PL** (2012) A novel wideband bandpass filter using open stubs multi-mode square ring resonator. In *The 2012 International Conference on Advanced Technologies for Communications*, Ha Noi, Vietnam, 180–182.
14. **Roberg M and Campbell C** (2013) A novel even & odd-mode symmetric circuit decomposition method. In *2013 IEEE Compound Semiconductor Integrated Circuit Symposium (CSICS)*, Monterey, CA, USA, 1–4.
15. **Gao K, Cao X, Gao J, Li T, Yang H and Li S** (2022) Low-RCS metasurface antenna array design with improved radiation performance using odd- and even-mode analysis. *IEEE Antennas and Wireless Propagation Letters* **21**(2), 421–425.
16. **Pozar DM** (1998) *Microwave Engineering*, 2nd edn. New York, NY: Wiley.
17. **Chen K and Peroulis D** (2012) Design of broadband highly efficient harmonic-tuned power amplifier using in-band continuous Class-F^{-1}/F mode transferring. *IEEE Transactions on Microwave Theory & Techniques* **60**(12), 4107–4116.
18. **Sadeque MG, Yusoff Z, Hashim SJ, Marzuki ASM, Lees J and FitzPatrick D** (2022) Design of wideband continuous Class-F power amplifier using low pass matching technique and harmonic tuning network. *IEEE Access* **10**, 92571–92582.
19. **Tamrakar V, Dhar S, Sharma T and Mukherjee J** (2022) Investigation of input-output waveform engineered high-efficiency broadband Class B/J power amplifier. *IEEE Access* **10**, 128408–128423.
20. **Dhar SK, Sharma T, Darraji R, Holmes DG, Illath SV, Mallette V and Ghannouchi FM** (2019) Investigation of input–output waveform engineered continuous inverse Class F power amplifiers. *IEEE Transactions on Microwave Theory & Techniques* **67**(9), 3547–3561.

Luyu Zhang is pursuing her bachelor's degree in Electronic Information Engineering at Hangzhou Dianzi University, Hangzhou, China. Her current research interests include the design of microwave power amplifiers and radio frequency rectifiers.

Zhiwei Zhang received the B.S. degree and the Ph.D. degree in Electronic Science and Technology from Hangzhou Dianzi University, Hangzhou, China, in 2017 and 2022, respectively. He was with the Centre for Wireless Innovation, ECIT Institute, Queen's University Belfast, as a visiting student from 2020 to 2021. He is currently an associate professor with Hangzhou Dianzi University. His current research interests include highly linear and efficient microwave PA design.

Chenlu Wang is currently studying for her undergraduate degree in Electronic Information Engineering at Hangzhou Dianzi University, Hangzhou, China. Her research focus includes the design of microwave power amplifiers and radio frequency rectifiers.

Chao Gu received the B.Sc. and M.Sc. degrees from Xidian University, Xi'an, China, in 2009 and 2012, respectively, and the Ph.D. degree from the University of Kent, Canterbury, U.K., in 2017. He is currently with the Centre for Wireless Innovation, ECIT Institute, School of Electronics, Electrical Engineering and Computer Science, Queen's University Belfast, Belfast, U.K. His research interests include phased array antennas, reconfigurable antennas, and frequency selective surfaces.